Comparison of Thermal Variance Dissipation Rates from Moored and Profiling Instruments at the Equator

A. PERLIN AND J. N. MOUM

College of Earth, Ocean and Atmospheric Sciences, Oregon State University, Corvallis, Oregon

ABSTRACT

As a quantitative test of moored mixing measurements using χpods, a comparison experiment was conducted at 0°, 140°W in October–November 2008. The following three measurement elements were involved: (i) NOAA's Tropical Atmosphere Ocean (TAO) mooring with five χpods, (ii) a similar mooring 9 km away with seven χpods, and (iii) Chameleon turbulence profiles at an intermediate location.

Dissipation rates of temperature variance and turbulent kinetic energy are compared. In all but 3 of 17 direct comparisons 15-day mean values of χ_T agreed within 95% bootstrap confidence limits computed with the conservative assumption that individual 1-min χpod averages and individual Chameleon profiles are independent. However, significant mean differences occur on 2-day averages. Averaging in time reduces the range (95%) in the observed differences at two locations from a factor of 17 at 1-day averaging time to less than a factor of 2 at 15 days, presumably reflecting the natural variability in both the turbulence and the small-scale fluid dynamics that lead to instability and turbulence.

The motion of χpod on a mooring beneath a surface buoy is complex and requires a complete motion package to define in detail. However, perfect knowledge of the motion of the sensor tip is not necessary to obtain a reasonable measure of χ_T. A sampling test indicated that the most important motion sensor is a pressure sensor sampled rapidly enough to resolve the surface wave–induced motion.

1. Introduction

Temporal variations in mixing at a fixed location may cover many orders of magnitude driven by large-scale dynamics with long or intermittent periodicity. For example, although several shipboard experiments in the central equatorial Pacific beginning in 1984 had indicated variability in mixing associated with the daily heating cycle (Gregg et al. 1985; Moum and Caldwell 1985), shear instabilities (Moum et al. 2011), and Kelvin waves (Lien et al. 1995), it was not until 2008 that the dominating contribution to sea surface cooling via mixing of cool fluid from below, associated with tropical instability waves, was quantified (Moum et al. 2009); and that was by happenstance. It is more likely than not that all of the modes of variability in mixing at the equator have yet to be established. Foremost among these would be the role of mixing as feedback to ENSO-related phenomena.

To sample turbulence (considered here as the mechanical contributor to mixing) over the long periods of time necessary to resolve its effect on long time-scale phenomena requires new methods to make long time series measurements. This has been successfully done in several limited cases. Williams et al. (1987) used acoustic travel time sensors on a large ocean bottom array. Doron et al. (2001) deployed a particle imaging velocimeter on the seafloor. Wiles et al. (2006) computed structure functions from a well-resolved bottom-mounted acoustic Doppler current profiler, while Lorke and Wuest (2005) scaled the inertial subrange of velocity measurements from a pulsed coherent acoustic Doppler current profiler, and Moum et al. (2007) did the same with acoustic Doppler velocimeter measurements. McPhee (1992) used ducted rotors together with a temperature and conductivity sensor to make eddy covariance flux measurements in the upper ocean beneath the sea ice. In all of these examples, the instrument platform was rigidly fixed to either the seafloor or to ice.

Corresponding author address: A. Perlin, College of Earth, Ocean and Atmospheric Sciences, Oregon State University, Corvallis, OR 97331.
E-mail: aperlin@coas.oregonstate.edu

The difficulties in making turbulence measurements on oceanographic moorings are indicated by the relative lack of such measurements. A one-of-a-kind device developed by Lueck et al. (1997) saw limited though intriguing use in inland tidal channels on a mooring buoyantly suspended from the seafloor. Only a portion of the data could be saved from deployments in the early 1990s.

Surface moorings in the open ocean are continually pumped by surface waves that transmit a range of motions down the cable (Moum and Nash 2009). To gain a complete understanding of these motions and how they affect the environmental signal requires a full suite of acceleration measurements, preferably oversampled and stored for further analysis. Only recently have we been able to reap the benefits of technical advances that have accompanied cellular telephones and digital cameras; low-power, surface-mounted electronics, high-capacity batteries, and extensive data storage using solid-state storage devices. These advances have permitted development of χpods, vaned, internally recording instruments that measure temperature at 10 Hz and temperature gradients at 120 Hz using fast thermistors (Moum and Nash 2009). They were designed with the intention of deployment on oceanographic moorings for periods of 1 year. We have maintained a near-continuous deployment of 3–6 χpods in the upper equatorial Pacific on National Oceanic and Atmospheric Administration's (NOAA's) Tropical Atmosphere Ocean (TAO) mooring at 0°, 140°W since September 2005. From these records is emerging a new perspective of both the details and long-term variability of mixing and the internal wave field in the equatorial ocean (Moum et al. 2011).

To the end of 2010, we have obtained 208 χpod-months of data at various depths on the 0°, 140°W mooring from 326 χpod months of deployments. Failures have been primarily due to the following:

- Broken sensors: The χpods measure temperature with bare thermistors in order to sense the small, turbulent scales of the temperature field. Initial deployments were made with unprotected sensors, which lasted several weeks–months before mechanical breakage. We believe this is due to fish schooling at the mooring. Protection of the bare thermistor with a simple cage (Moum and Nash 2009) has nearly eliminated sensor breakage.
- Spent batteries: Since we began our deployments, the schedule for turning the buoys around has changed from 6 to 12 months and has on one occasion slipped to 18 months, during which all of our units ran out of power. The batteries we have been using have largely met manufacturer's specification.

TABLE 1. The χpod deployment depth (m).

NOAA TAO mooring	EQUIX mooring
18	24
58	28
75	49
111	51
135	53
	62
	80

- Unknown causes: Presumably there have been manufacturing flaws where wiring harnesses, for example, have not been robust enough.[1]
- Lost moorings: On two separate occasions, the mooring has broken free. On one occasion, the mooring was recovered and we have a nice record from the drifting mooring. On the other occasion, all of the gear was simply lost.

A central objective in this development has been quantification of the thermal variance dissipation rate χ_T from the measured temperature gradients. From this is derived an estimate of the turbulent kinetic energy dissipation rate ϵ and the turbulence diffusion coefficient K_T. We have made qualitative comparisons to historical equatorial datasets (Moum and Nash 2009), as well as to independent estimates from the low wavenumber range of temperature gradient spectra (Zhang and Moum 2010).

The comparisons noted above are less satisfactory than can be made by real-time comparison to fully independent estimates derived from our turbulence profiler, Chameleon (Moum et al. 1995). In part to evaluate χpod estimates of χ_T, an experiment was conducted near NOAA's TAO mooring at 0°, 140°W. This TAO mooring was equipped with χpods at depths ranging from 18 to 135 m (Table 1). An additional mooring was deployed 9 km north of the TAO mooring by colleagues from the University of Washington (Fig. 1). This second mooring included a dense array of velocity, conductivity, and temperature sensors to investigate the details of the internal wave field at the equator, as well as χpods at depths ranging from 24 to 80 m (Table 1). Following deployment, the ship occupied a station between the two moorings for a period of 15 days, which corresponded to a ¾ cycle of a tropical instability wave (TIW) (Moum et al. 2009), while conducting more than 2600 turbulence profiles.

Turbulence measurements from instruments moored beneath a surface-following float differ from those from

---

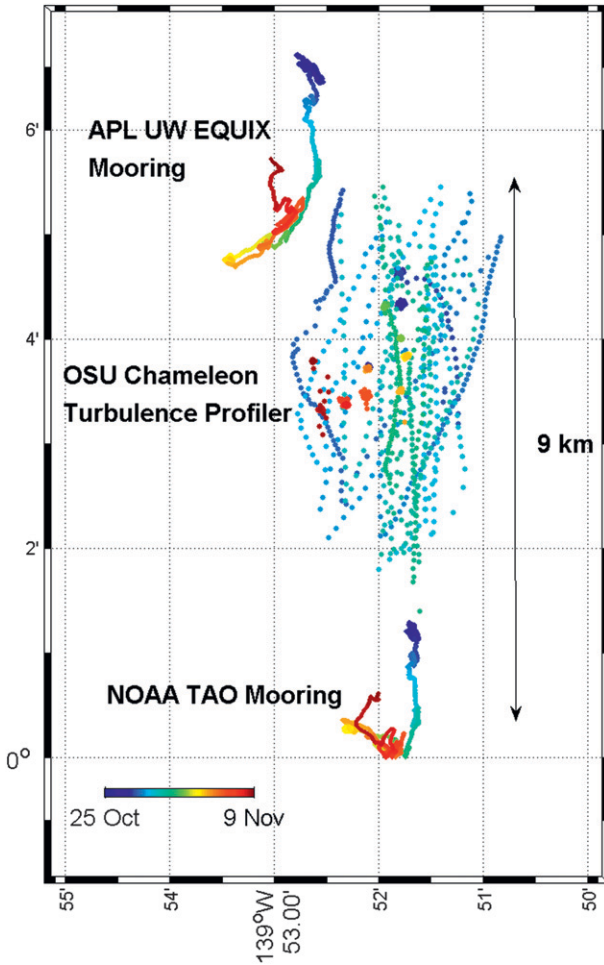[1] All manufacturing is done in our laboratory.

FIG. 1. Positions of moorings and Chameleon profiler over 15 days at 0°, 140°W. (bottom left) The color coding reflects time.

TABLE 2. Notation.

Symbol	Explanation
BCS	Body coordinate system (see Fig. A1)
ENU	Earth coordinate system (east, north, up)
$A_{x,y,z}$	Measured components of total acceleration in BCS
$A_{x,y,z}^g$	Components of gravitational acceleration in BCS
$A_{x,y}^{lp}$	Low-passed $A_{x,y}$
D_T	Thermal diffusivity
α	Thermal expansion coefficient
$d_{1x,y,z}$	Distance from upper sensor tip to the corresponding axis
$d_{2x,y,z}$	Distance from lower sensor tip to the corresponding axis
f	Frequency
g	Gravitational acceleration
J_q	Total heat flux
K_T	Turbulence diffusion coefficient
N^2	Buoyancy frequency squared
P	Pressure
Pitch	Inclination angle (tilt in the direction of the χpod's heading)
pitch$_{lp}$	Low-passed pitch
Roll	Bank angle (tilt in the direction normal to the χpod's heading)
roll$_{lp}$	Low-passed roll
R_{rpy}	Yaw–pitch–roll directional cosine matrix (DCM)
$R_{roll,pitch,yaw}$	Roll DCM, pitch DCM, yaw DCM
S^2	Velocity shear squared
t	Time
T	Temperature
T_t	Time derivative of temperature
T_x	Horizontal derivative of temperature
U, V, W	Components of current velocity in ENU
U^B, V^B, W^B	Components of current velocity in BCS
u	Flow speed past sensor
$u_{1,2,3,4}$	Flow speed past sensor in tests 1–4
u_a, v_a, w_a	Components of motion package velocity in BCS
u_c, v_c, w_c	Components of sensor tip velocity in BCS
X, Y, Z	Axes of BCS originating at motion package
yaw	Heading angle (clockwise rotation around vertical axis from the east)
z_t	Time derivative of vertical position
χ_T	Thermal variation dissipation rate
$\chi_{T1,2,3,4}$	χ_T in tests 1–4
χ_T^{Cham}	χ_T from Chameleon
$\chi_T^{\chi pod}$	χ_T from χpod
ϵ	Turbulence kinetic energy dissipation rate
ϵ_χ	ϵ computed from χ_T
Φ_{T_x}	Frequency spectrum of T_x
Γ	Mixing efficiency
$\omega_{x,y,z}$	Components of angular velocity in BCS

a vertical profiler in two important aspects. First, while estimation of flow speed past the sensor for a freefalling profiler is relatively straightforward,[2] our upper-ocean χpods see a flow that is a combination of currents plus cable motion, requiring independent measurement of the cable motion. Second, while the profiler measures vertical gradients of scalar properties, χpods measure temporal gradients, from which we infer horizontal gradients.

The objective of this paper is to provide an assessment of our estimates of χ_T calculated from χpod measurements. This is done by statistical comparison of the three datasets. The measurements are described in more detail in section 2. Results of the comparisons are discussed in section 3, space–time variations in section 4, and uncertainties in section 5. These are followed by a summary in section 6. In the appendix, we define the χpod motion computations derived from accelerometers and angular rate sensors, including a description of the directional cosine matrix used for coordinate transformation. Table 2 provides a summary of the notations used in this paper.

---

[2] The flow speed is estimated from the rate of change of pressure where, generally, vertical velocities are small compared to the nominal fall rate of 1 m s^{-1}.

2. Measurements

Here, χ_T is defined from measured temperature gradient spectra as

$$\chi_T = 6D_T \int_0^\infty \Phi_{T_x}(f)\,df, \tag{1}$$

where D_T is the thermal diffusivity and $\Phi_{T_x}(f)$ is the frequency f spectrum of horizontal temperature gradient T_x, where T_x is estimated from the differentiated temperature signal T_t through Taylor's frozen flow hypothesis, $T_x = T_t/u$. Here, u is the flow speed past the sensor. In the reference frame of the profiler, we replace x with the vertical coordinate z and u with the time derivative of vertical position z_t. In the χpod reference frame, u includes contributions from mean currents and from the motion of the cable to which the χpod is attached, including χpod rotations about the cable. In practice, we scale $\Phi_{T_x}(f)$ to a universal wavenumber spectrum to estimate χ_T. Moum and Nash (2009) discuss the details of the spectral scaling used for the χpod analysis. Nash and Moum (1999) discuss the physical nature of the spectra.

By equating two forms of turbulence scalar diffusion coefficient (Osborn and Cox 1972; Osborn 1980), we estimate ϵ from χ_T as

$$\epsilon_\chi = \frac{N^2 \chi_T}{2\Gamma T_z^2}. \tag{2}$$

Here, $N^2 = -g\rho_z/\rho$ is the squared buoyancy frequency; g is the acceleration resulting from gravity; ρ is density; and T_z, ρ_z are vertical gradients of temperature and density, respectively. We assume $\Gamma = 0.2$ is a constant mixing efficiency.

a. Profiling

Chameleon (Moum et al. 1995) was deployed from Research Vessel (R/V) *Wecoma* at 0°, 140°W over the period from 24 October to 9 November 2008. During this period, profiles of temperature, salinity, ϵ, and χ_T were made to 200-m depth at the rate of 6–10 profiles per hour, interrupted only occasionally for repositioning. The track of the ship during this period is shown in Fig. 1. Velocity profiles were also made to 400-m depth using a combination of acoustic Doppler current profilers (hull-mounted 300- and 75-kHz profilers and a 150-kHz profiler mounted over the side of the vessel).

b. χpods on TAO mooring

In May 2008, prior to our field experiment, χpods were deployed by NOAA personnel from the NOAA ship *Ka'Imimioana* on the TAO mooring at 0°, 140°W. Deployment depths of the units are shown in Table 1. A GPS receiver/recorder was mounted on the surface float to record positions at 30-s intervals, yielding the mooring watch path shown in Fig. 1.

c. χpods on EQUIX mooring

An additional mooring, heavily instrumented in the upper 150 m, was deployed 9 km to the north of the TAO mooring by the Applied Physics Laboratory (APL) of the University of Washington (UW) group immediately prior to commencement of profiling as a part of a cooperative experiment to investigate the dynamics of high-frequency internal waves (R.-C. Lien and M. C. Gregg, APL/UW, 2008, personal communication). Deployment depths of χpods are shown in Table 1. A GPS receiver/recorder mounted on the surface float shows the mooring watch path (Fig. 1). The mooring was recovered following our profiling experiment; all data were downloaded and the mooring was redeployed through March 2009.

3. Results

This experiment provided an opportunity for an extensive comparison of turbulence measurements between moored and profiling platforms. As a basis for comparison, we first evaluate time series of χ_T at fixed depths using hourly averaged data pairs and then time-averaged vertical profiles of χ_T and ϵ.

a. Time series comparisons

An examination of hourly averaged, near-surface data (Fig. 2b) reveals several common features as well as some variations between measurements. The diurnal cycle (defined by the surface heat flux; see Fig. 2a) in near-surface mixing is clear in the signals from all three measurement platforms, as is a longer time-scale variation. The total range of all χ_T measurements are similar (from 10^{-9} to 10^{-5} K^2 s^{-1}; Fig. 2c), and the diurnal variations are approximately equivalent (~2 decades in χ_T). This was previously surmised indirectly by Moum and Nash (2009) by comparing near-surface χpod estimates of ϵ_χ and near-surface profiler measurements of ϵ from an earlier experiment at that location (Moum et al. 1995). The more direct comparison we have undertaken here is reassuring. There also are considerable differences between χpod and Chameleon estimates in the latter half of the record, where χpod estimates were significantly smaller. Unfortunately, the χpod at that depth on the EQUIX mooring failed during this period (2 November; Fig. 2b). Because the TAO χpod and
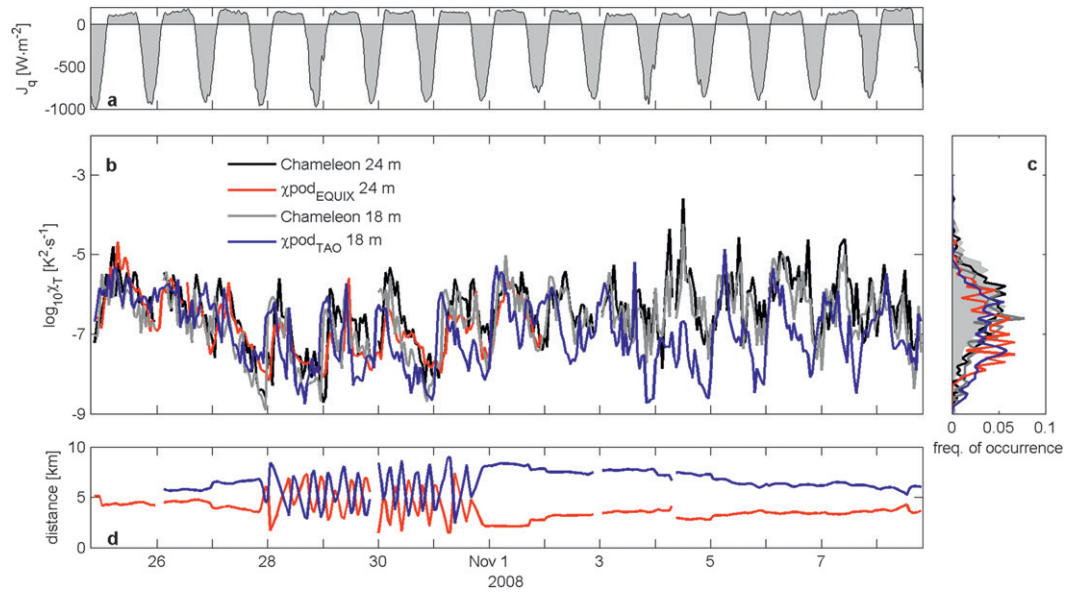
FIG. 2. (a) Surface heat flux as determined from bulk formulas using measurements from sensors aboard R/V *Wecoma*; (b) hourly means of χ_T from χpod (EQUIX mooring) at 24 m, χpod (TAO mooring) at 18 m, and Chameleon at 18 and 24 m; (c) distributions of these hourly means. The shaded area represents the averaged distribution shown in Fig. 3c; (d) distance between EQUIX mooring and *Wecoma* (red line) and TAO mooring and *Wecoma* (blue line).

Chameleon were separated by at least 5 km, it is possible that spatial variations are largely responsible for the differences.

At greater depth, immediately above the core of the Equatorial Undercurrent (EUC; 75–80 m; Fig. 3) no diurnal variation is noticeable. Time variations loosely related to the meridional current velocity (Fig. 3a), or perhaps the vertical shear (Fig. 3b), appear in all of the signals from that depth range. Distributions of χ_T compare reasonably well (Fig. 3d) despite the occasional large differences between measurements (on 7 November, e.g.).
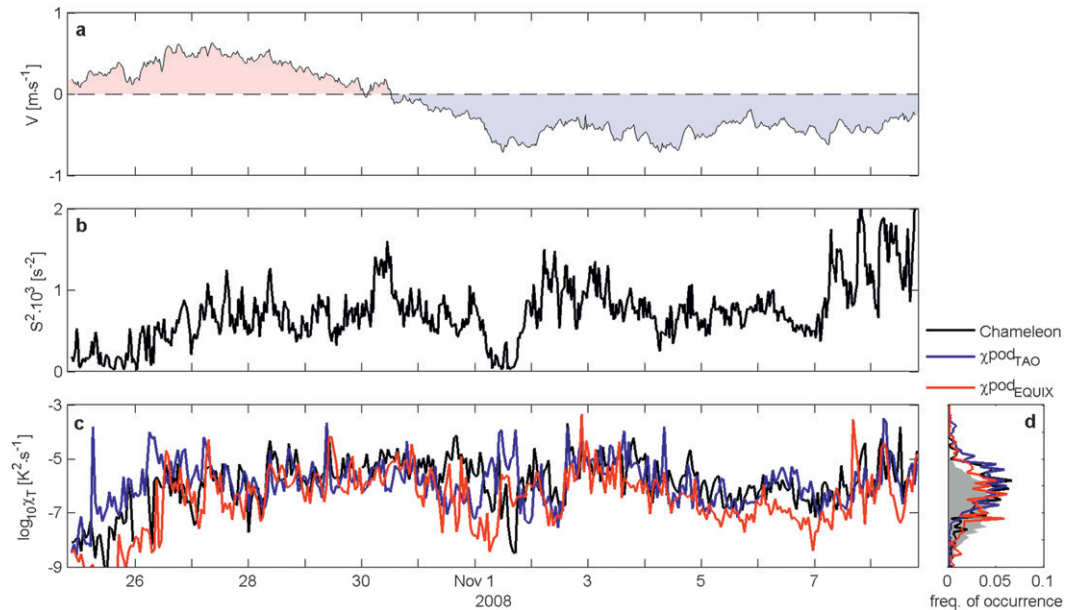

FIG. 3. (a) Meridional velocity at 76 m; (b) squared velocity shear at 76 m; (c) hourly means of χ_T from the EQUIX mooring χpod at 75 m, the TAO mooring χpod at 80 m, and Chameleon at 76 m; and (d) distributions of these hourly means. The shaded area represents the averaged distribution shown in Fig. 2c.
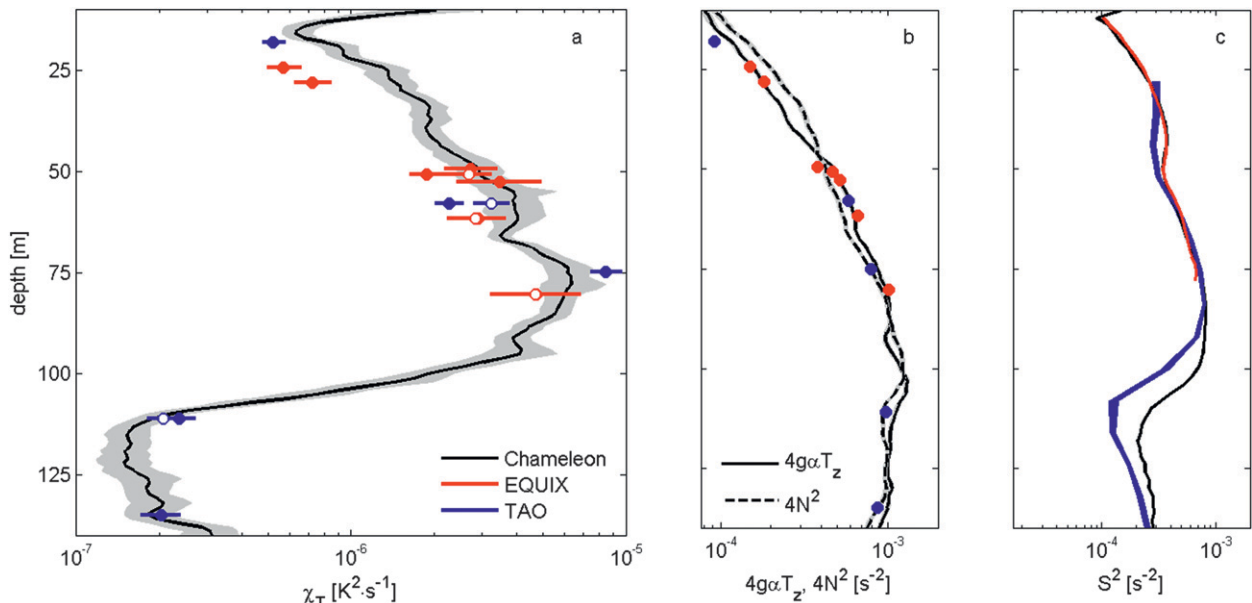
FIG. 4. (a) Comparison of χ_T estimates from χpod time series on EQUIX and TAO moorings and Chameleon turbulence profiler. Data were averaged over 15 days. The 95% bootstrap confidence limits for Chameleon data (gray shading) and χpod (horizontal bars) are indicated. Both χpod thermistors were operational for the entire averaging period and independent estimates from (presumably) nearly identical signals are compared; the second thermistor is represented (open circle). (b) Comparison of N^2 estimates. The $4N^2$ computed from temperature and conductivity measurements on Chameleon (dashed black line). The χpods measure only T and N^2 is estimated from the temperature contribution as $g\alpha T_z$ alone (solid line). (c) Vertical profiles of S^2 at the three locations are shown.

b. Averaged χ_T profiles

Averages of χ_T from χpods and Chameleon over the entire 15-day period (actually 15½ days) are indistinguishable within 95% confidence intervals for 14 out of 17 χpod sensors (Fig. 4a). Estimates from the second thermistors on the χpods, when available, are considered independent. Confidence intervals for Chameleon were computed using bootstrap statistics on 1-m vertical averages, using all individual 2624 Chameleon profiles. Confidence intervals for χpods were computed from 1-min χ_T averages, again using boostrap statistics. There is no difference between moored and Chameleon estimates (within 95% confidence intervals) at 18, 49, 51, 53, 58 (upper sensor), 62, 75, 80, 111, and 135 m. Moored measurements are smaller than profiling measurements (the upper limit of the moored confidence interval and the lower limit of the profiling confidence interval) by about 36% at 24 m (only the upper sensor data), 22% at 28 m (only the upper sensor data), and 22% at 58 m (for the lower sensor).

All instruments reflect a strong depth dependence in χ_T. Near the surface, $\chi_T \sim 10^{-6}$ K^2 s^{-1}. Immediately above the EUC core, $\chi_T \sim 10^{-5}$ K^2 s^{-1}, and at depths >110 m χ_T decreased to $\sim 2 \times 10^{-7}$ K^2 s^{-1}. This structure represents the most intense mixing yet observed at the equator (Moum et al. 2009) and is associated with the passage of a TIW that enhances the EUC shear

through a strong wave-induced meridional component. The enhanced mixing above 100 m and reduced mixing below 110 m is sensed by all of the instruments at all measurement sites.

Our estimation of confidence intervals is likely conservative. The number of degrees of freedom (DOF) for 1-min χpod estimates over the 15-day period is approximately 23 000, which is roughly 10 times the number of DOF assigned to Chameleon estimates at fixed depths. Yet, at least in the upper 40 m, variability is associated with the daily heating cycle, suggesting that the DOF over a 15-day period is considerably smaller. If, instead, we assume that ½-day averages are independent, the diurnal cycle is resolved, then DOF = 31 and 95% confidence intervals overlap at all depths. This assumption is certainly too liberal and the appropriate confidence intervals lie somewhere in between. In any case, however, the final result is that individual estimates agree to within a factor of 2 (Fig. 4a), a measure of agreement that we consider to be extremely heartening.

As part of the iterative procedure to scale the temperature gradient spectrum, ϵ_χ is estimated via Eq. (2). A contribution to any bias in our estimates of χ_T comes from the lack of salinity measurement on χpods. For these measurements, we estimate N^2 from the temperature contribution alone, $g\alpha T_z$ (Fig. 4b).
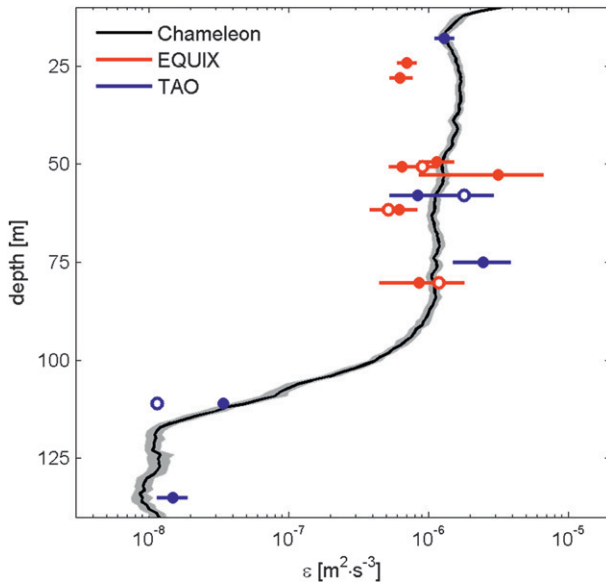
FIG. 5. The χpod estimates of ϵ_χ compared with profiler estimates of ϵ from airfoil probe measurements on Chameleon. The 95% bootstrap confidence limits for Chameleon data (gray shading) and for χpod (horizontal bars) are represented. Where both χpod thermistors were operational for the entire averaging period, independent estimates from (presumably) nearly identical signals are compared, and the second thermistor is represented (open circle).

c. Averaged ϵ profiles

We also compared vertical profiles of ϵ_χ estimated from χpod measurements of χ_T using (2) with ϵ computed from Chameleon airfoil probe measurements (Fig. 5). Estimates from 10 of 17 χpod sensors agree within 95% bootstrap confidence limits. The 15-day averages show very high values in the upper 80 m and a reduction by two orders of magnitude below 100 m. The apparent bias at 24 m, 28 m may be partially attributed (30%) to the low χpod estimate of N^2 using $g\alpha T_z$ in that depth range (Fig. 4b). This contributes to ϵ_χ via Eq. (2).

4. Variations in space and time

While 15-day averages of χ_T at fixed depths agree within a factor of 2 (worst case), occasional large differences in averaged values of χ_T are apparent on shorter time scales. For example, 2-day averages (Fig. 6) indicate good agreement, within a factor of 2 or so, during some averaging intervals (26–27 October, 1–2 November, and 7–8 November), but poor agreement during others (30–31 October and 5–6 November), when some averaged values, which are in agreement at intervals both preceding and after, differ by more than a factor of 10. Differences occur over significant periods of time during which χpod estimates of χ_T both exceed (24–25

October) and are less than (30–31 October) the Chameleon estimates. The agreement in 15-day mean values yet variability on daily time scales is similar to comparisons of ϵ from two sets of profiling measurements made at this same location in 1991 (Moum et al. 1995). Here, we consider spatial and temporal variations independently.

To produce data pairs for statistical comparison, we computed hourly averages of χ_T from each χpod time series. We averaged the Chameleon profile data ± 1.5 m about each χpod depth and averaged for 1 h (equivalent to 6–10 profiles). In Fig. 7 we show distributions of χ_T from one depth (near 60 m); this represents the smallest depth difference between any of the χpods on the two moorings, thereby permitting a three-way comparison. The result indicates that roughly 40% of the hourly data pairs are within a factor of 3 of each other and 70% are within a factor of 10 (Fig. 7).

a. Spatial variations

Linear correlations were computed between hourly data pairs as a function of separation distance. Positions of moorings and the ship were used to subsample data pairs corresponding to separations between the ship and moorings of 1.5–4 and 6–8.5 km. Only data from the time period 28–31 October were considered, because the ship moved continuously back and forth between the two moorings, while staying mostly stationary the remainder of the time (Fig. 2d). In addition, correlations were computed between hourly data pairs from both moorings for the entire time period using χpods deployed at approximately similar depths. Moorings were separated by ≈9 km. The comparison is summarized in Fig. 8. Correlations for near-surface (18–28 m) units were significant in all cases. Presumably the coherence of large-scale atmospheric forcing is responsible, primarily in the form of the diurnal heating/cooling cycle. For χpods deployed at middepth (49–62 and 75–80 m) correlations were significant at smaller (<4 km) separations and insignificant at larger (>6 km) separations, suggesting a decorrelation scale for turbulent events, or at least for forcing of turbulence events, between 4 and 6 km. Finally, there was no correlation for χpods deployed below 100 m, suggesting decorrelation over distances smaller than 4 km.

b. Temporal variations

Even though 15-day mean values suggest that long time-scale variability is coherent over that period, decorrelation between physically separated measurements exists at short time scales. Figure 6 demonstrates that on 2-day periods χ_T at one site can differ from χ_T at another site by a factor of 10, but that longer averaging reduces differences between sites (Fig. 4a).

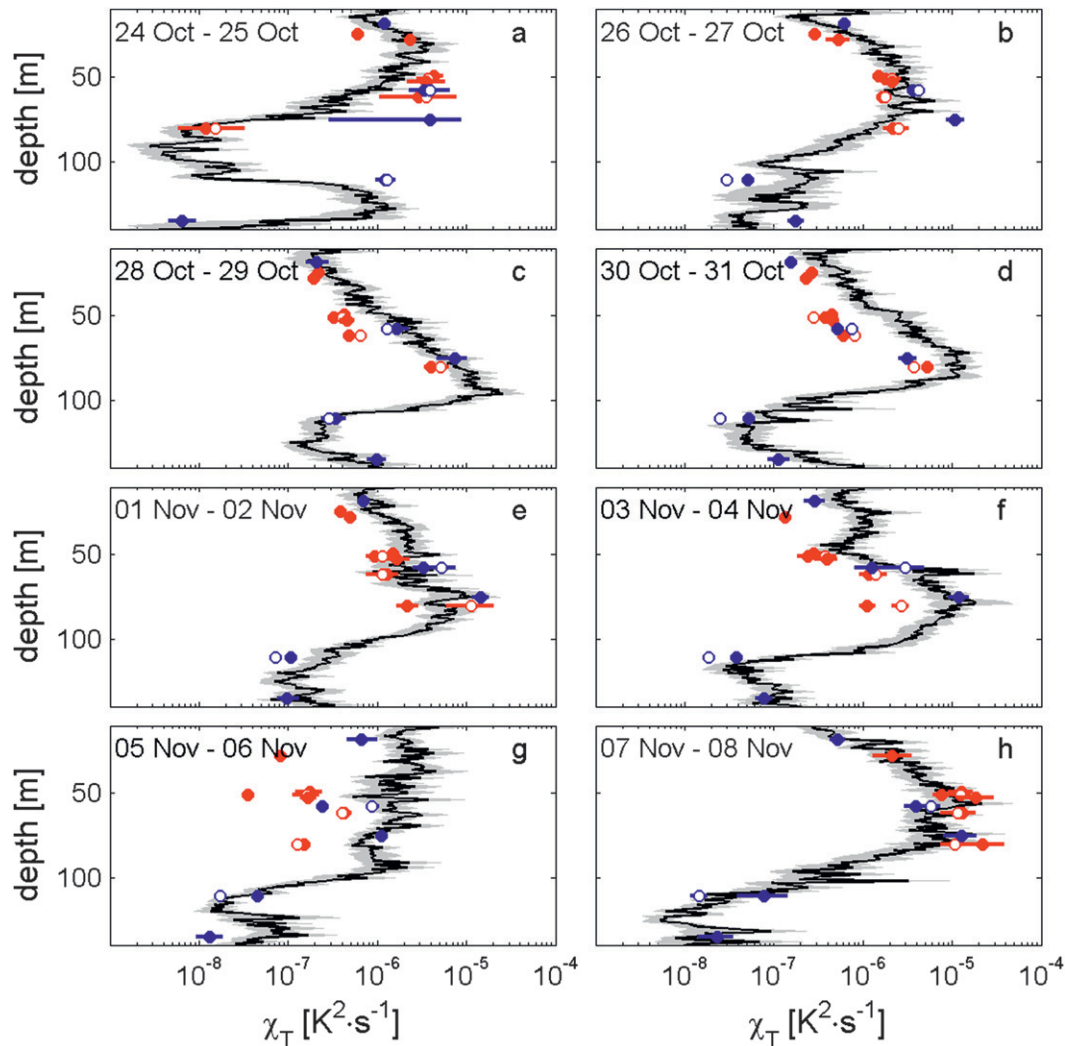FIG. 6. (a)–(h) Comparison of χ_T estimates from χpods on EQUIX and TAO moorings and Chameleon turbulence profiler. Data were averaged over 2 days. Symbols and colors are the same as in Fig. 4.

If natural variability is the main reason for differences between estimates, then increasing the averaging periods should reduce this. To test this hypothesis we calculated the ratio $\chi_T^{\chi\text{pod}}/\chi_T^{\text{Cham}}$ for each χpod unit, varying the averaging period between ½ and 15 days. Figure 9a shows how both the range of distribution of the ratio is reduced and the bias as represented by the median of the ratio that converges to 1 as averaging period increases. More importantly, the 95% range of values is reduced from a factor of 23 at averaging periods of ½ day to less than a factor of 2 at the 15-day averaging period (Fig. 9b).

5. Uncertainties

Moum and Nash (2009) examined the contributions of uncertainties on various fundamental quantities to

uncertainty in χpod estimates of χ_T. In the comparisons discussed here, another factor appears. This is the relative uncertainty in depths of χpods and Chameleon, estimates from which comparisons are made to each other. This may contribute a considerable bias in comparisons at depths where χ_T has significant depth dependence. In addition, because of the recognized importance of package motion in the measurement, recent deployments have included a suite of three linear accelerometers plus three angular rate sensors from which the full package motion is computed. These permit a more complete assessment of the role of the total flow speed past the sensor tip in our uncertainty in χ_T than could be evaluated by Moum and Nash (2009).

a. Relative depths

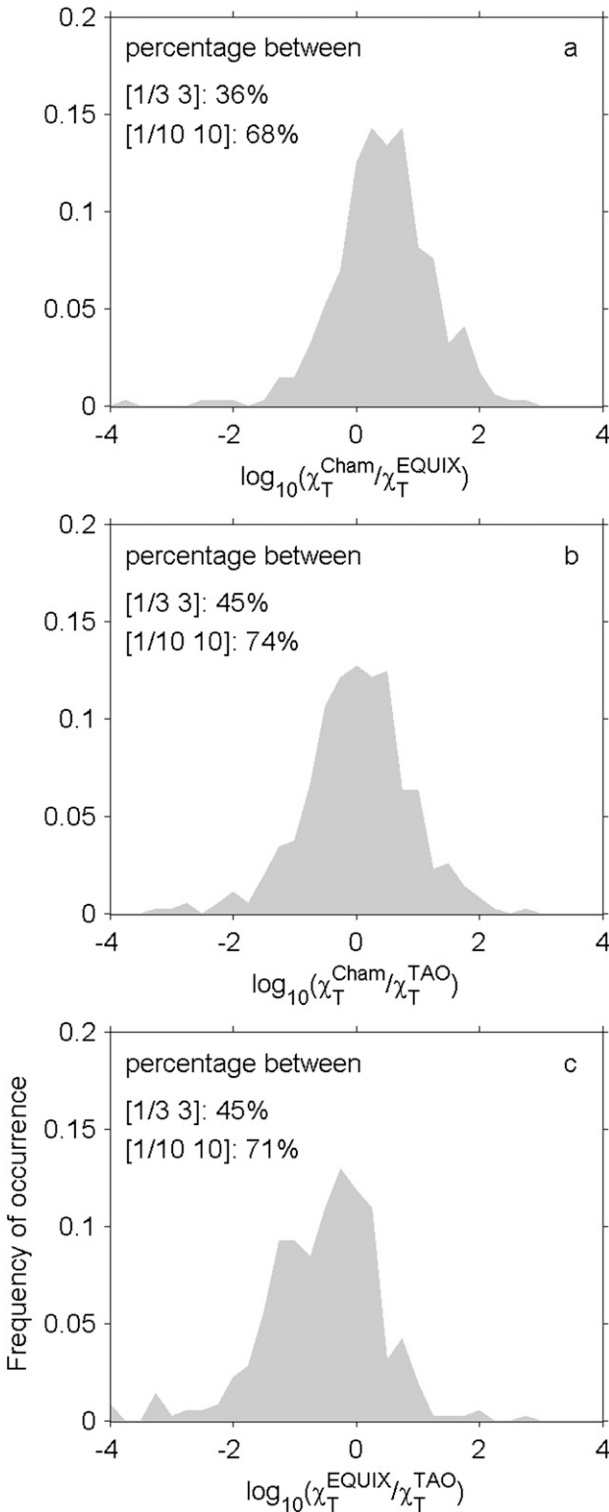Figure 4 demonstrates that in regions of strong gradients (i.e., 80–115 m) a small change in depth may
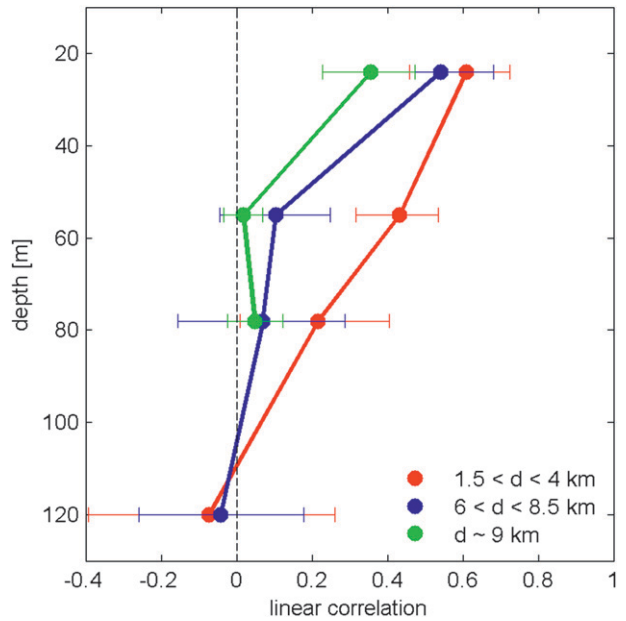
FIG. 8. Linear correlation coefficients computed between Chameleon–χpod pairs (1-h averages) as a function of spatial separation. The distance separating pairs is indicated by the symbol/line color: pairs with separation between 1.5 and 4 km (red), and pairs with separation between 6 and 8.5 km (blue). These correlations were computed for Chameleon mooring pairs for the time period when the ship moved continuously between the two moorings (last 4 days of October). Correlations for pairs with separation of 9 km are shown (green), corresponding to χpods deployed at approximately similar depths on two moorings for the entire time period. The 95% bootstrap confidence limits are shown with horizontal bars.

FIG. 7. Distributions of ratios of χ_T estimates (a) at 62 m from Chameleon and EQUIX χpod data, (b) at 58 m from Chameleon and TAO χpod data, and (c) at 62 m from EQUIX χpod and 58 m from TAO χpod data.

result in a large change in turbulence properties. This means that χ_T differences between data pairs may in part be due to relative inaccuracies in our measurement of the depths of χpod sensors and of Chameleon. A simple way to test the sensitivity of the data pair comparison to uncertainty in the depth is to compare χ_T estimates from two instruments with Chameleon data from different depth bins (because we have continuous vertical profiles with that instrument). Uncertainty resulting from the calibration of an individual pressure sensor may reach ± 2 m for each instrument, therefore cumulative depth uncertainty could be ± 4 m. Figure 10 shows the ratios $\chi_T^{Cham}/\chi_T^{\chi pod}$ using Chameleon estimates in a range ± 10 m from our best estimate of χpod depths (± 4 m shown with a thick line). In most cases depth uncertainty ± 4 m results in less than a factor of 2 difference between two χ_T estimates, but in regions of high gradients (110 m, e.g.), depth uncertainty within ± 4 m results in a factor of 4 difference, while uncertainty within ± 10 m may result in over an order of magnitude difference.
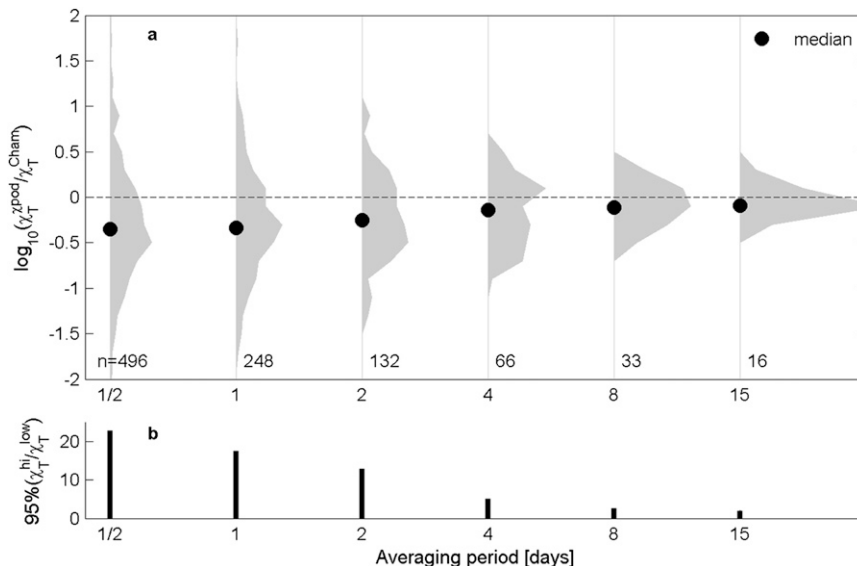
FIG. 9. Temporal variability. (a) Distributions of $\chi_T^{\chi\text{pod}}/\chi_T^{\text{Cham}}$ computed for each χpod. The χ_T values in each estimate were averaged over periods from ½ to 15 days; n is the number of independent estimates in each distribution. The distribution medians are indicated (circle); (b) 95% limit of observed ratios of high to low χ_T at two locations as a function of averaging period.

b. Flow speeds

A complete determination of the flow speed past the sensor tip requires information not only of the current speed and the sensor tip's orientation relative to the current, but also the full motion of the sensor tip. This requires measurement of linear accelerations plus angular rates in three orthogonal coordinate directions. Together with the pressure sensor and compass, this constitutes a complete motion package, which is used to determine flow speed past the tip as in appendix A. While all χpods have a pressure sensor, a compass, and three-axis linear accelerometers, we have added angular rate sensors only for this specific test and use 24 h of data from another deployment at the same location.

Here we use the 24-h record of 1-s estimates (86 400 independent estimates in all) to determine uncertainties in both u and χ_T as a function of progressively limiting our ability to measure the complete speed of the flow past the sensor tip. We first compute u (as in appendix A) and χ_T using all available data and refer to this as our reference case. We then successively limit the information available to compute u, and hence χ_T, by removing 1) angular rate data 2) angular rate + compass data; 3) angular rate, compass + accelerometer data, thus leaving only the pressure sensor to detect vertical motion of the χpod on the cable; and 4) angular rate, compass, accelerometer + pressure data; in this case, u is simply the current speed.

In case 1 (with no angular rate sensors) the flow speed past the sensor is computed as

$$u_1 = [(u_s - U^B)^2 + (v_s - V^B)^2 + (w_s - W^B)^2]^{1/2}, \quad (3)$$

where U^B, V^B, and W^B are components of current speed in χpod coordinate system [body coordinate system (BCS)] and u_s, v_s, w_s are components of sensor speed in BCS. This is the same equation as reference case (A8), but χpod rotation angles for estimation of u_s, v_s, w_s and U^B, V^B, W^B are computed without the rate sensor's data, neglecting high-frequency tilts, and using only compass data for heading calculations (see appendix A for details of the U^B, V^B, W^B and u_s, v_s, w_s calculations). In effect, this means that the gravitational terms A_x^g, A_y^g, A_z^g (A3) are not properly determined.

In case 2 (with no angular rate sensors and no compass) we retain most of the information about χpod motion (including mean χpod tilts from accelerometers), but we do not know χpod's orientation relative to currents. We eliminate all data where the current speed is less than 0.05 m s^{-1} and assume that, for the remainder of the data, χpod's sensor tip is always oriented into the current. Under this assumption U^B is negative of the magnitude of the horizontal current velocity and $V^B = 0$,

$$u_2 = \{[u_s + \text{sqrt}(U^2 + V^2)]^2 + v_s^2 + (w_s - W^B)^2\}^{1/2}. \quad (4)$$
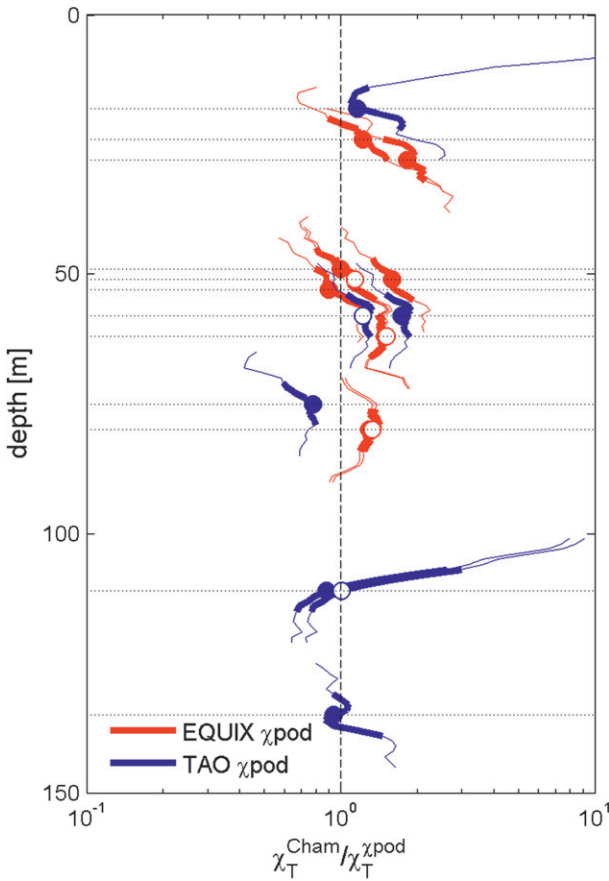
FIG. 10. Uncertainty in relative depths. Ratio $\chi_T^{\text{Cham}}/\chi_T^{\chi\text{pod}}$ using Chameleon estimates in a range ± 10 m from our best estimate of χpods depth (± 4 m shown with a thick line).

For case 3 we also assume that we have no accelerometer data, so we cannot calculate χpod's horizontal motion, while the pressure sensor is used to determine vertical motion,

$$u_3 = [U^2 + V^2 + (w_s - W)^2]^{1/2}. \quad (5)$$

Finally, if we exclude pressure data we arrive at case 4, in which our estimate of u is limited to the measured current speed,

$$u_4 = (U^2 + V^2 + W^2)^{1/2}. \quad (6)$$

Our comparison of the reference case with each of the four reduced-information cases is shown in Fig. 11. In case 1, the flow speed differs because of the inability to compute A_x^g, A_y^g, A_z^g at all frequencies (particularly in this case, with the surface wave band of frequencies).

In case 2, the assumption that the sensor tips completely point into the flow is also applied, which is not

correct at all times, leading to an additional difference in speed estimate from the reference value. The difference in speeds from the reference case is 15% in the mean, and the relative difference in χ_T is at most 7% in the mean.

In case 3, the removal of the accelerometer information from the speed estimate means that the pressure sensor is the only source of package speed (in this case, providing only the vertical component). Here the bias is larger and the speed estimates are lower by 13% in the mean, while χ_T estimates are biased high at 17% in the mean.

In case 4, relying only on the current speed yields a poor estimate of speed past the sensor tip, but the bias in estimates of χ_T is less than a factor of 2 in the mean.

The χpods installed on both moorings during the 15-day experiment used for comparison here were outfitted with accelerometers, a compass, and pressure sensors, but no rate sensors. Based on the above analysis we conclude that a lack of rotation rate data was insufficient to cause any noticeable bias in χ_T estimations. It should be noted that data used for the analysis were collected in strong current environment. Inevitably, information about χpod motion gains more importance in weak current environment.

6. Discussion and summary

This experiment was designed in part to provide a basis for assessing our techniques for quantifying χ_T (and ϵ_χ) from χpods on equatorial moorings. The three measurement sites were located by GPS and within a 9-km total separation. Recording positions at 30-s intervals provided detailed information on mooring watch paths (Fig. 1).

Magnitudes and vertical structure of both χ_T and ϵ_χ derived from χpods on the two moorings are in excellent agreement with estimates from Chameleon when averaged over the duration of the 15-day experiment (Figs. 4 and 5). In all but 3 of 17 direct comparisons at various depths, mean values of χ_T agreed within 95% confidence limits. Elsewhere, differences in mean values were less than a factor of 2.

However, large mean differences do appear when vertical profiles are averaged over 2-day time scales (Fig. 6). Further averaging in time serves to reduce the range (95%) in observed differences at two locations from a factor of about 17 at 1-day averaging time to less than a factor of 2 at 15 days (Fig. 9).

We attempted to assess spatial variability through correlations of hourly data pairs as a function of spatial separation. Significant, near-surface correlations are likely dominated by the strong daily variations in
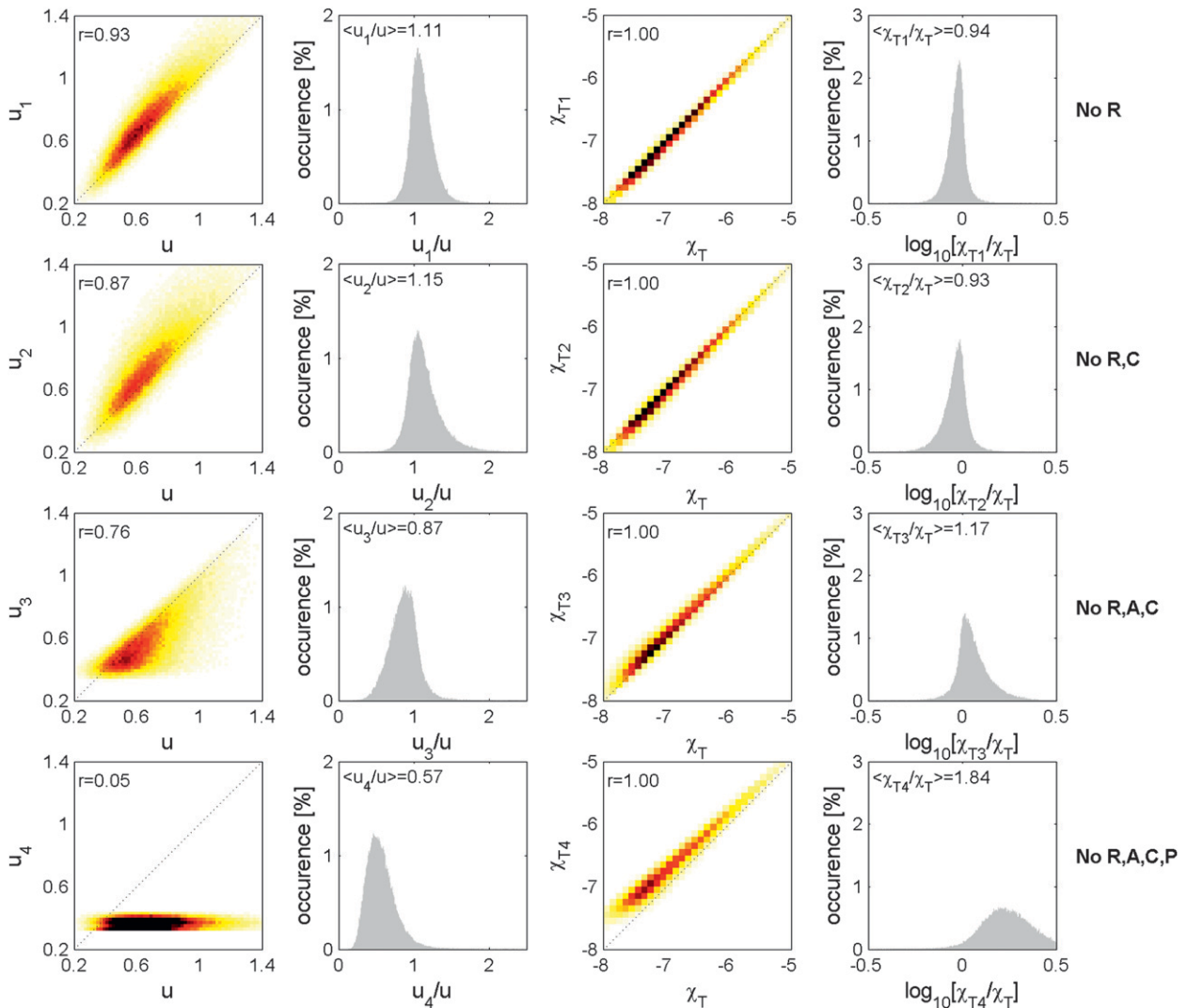
FIG. 11. Comparison of χ_T calculated with a limited number of motion sensors with χ_T calculated with full motion package. (from top to bottom) 1) No rotation rate sensors; 2) no rotation rate sensors and compass; 3) no rotation rate sensors, compass, and accelerometers; and 4) no rotation rate sensors, compass, accelerometers, and pressure sensors. (from left to right) 1) Flow velocity past the sensor calculated for the test case vs flow velocity past the sensor calculated with full motion package (correlation coefficient with 95% bootstrapped confidence limits on the top); 2) distribution of the ratio of the velocities (mean value with 95% bootstrapped confidence limits on the top); 3) χ_T calculated for test case vs χ_T calculated with full motion package (correlation coefficient with 95% bootstrapped confidence limits on the top); and 4) χ_T ratio distribution (mean value with 95% bootstrapped confidence limits on the top). The color coding represents frequency of occurrence, blacks being most frequently occurring.

atmospheric forcing that create daily mixed layer shallowing/deepening and coincident variation in upper-ocean mixing (Moum et al. 2009, e.g.). Uncorrelated data pairs at 120 m likely reflect the intermittent generation of shear instabilities below the core of the Equatorial Undercurrent, unassociated with surface forcing.

Natural geophysical variability of small-scale processes may appear as both spatial and temporal variability. These are almost impossible to distinguish in the absence of a fully resolved space–time field. We have

attempted to evaluate the variability, first as a function of spatial separation between measurement points and then as a function of averaging interval. If this variability is reduced by averaging in time or by smaller separation between observation points, then we expect that observed variations between data pairs are due to natural variability. This variability may be solely due to incomplete resolution of the turbulence. For example, Chameleon profiles yield 6–10 point estimates averaged into 1-h bins. These are then compared to χpod averages, which are derived from continuous time series.

This variability may also be due to real differences in the instabilities leading to turbulence. Indeed, it appears that shear instability is a critical factor in generating turbulence in this environment (Sun et al. 1998; Lien et al. 2002), the scales of which are significantly smaller than the spatial separations between measurements considered here (Moum et al. 2011).

Uncertainties in relative depths of χpods lead to a degradation in correlations. Uncertainty of as little as a few meters between two measuring instruments can result in significant differences in χ_T in regions where turbulence gradients are strong (section 5a).

The motion of χpods on moorings beneath a surface buoy is complex and requires a complete motion package to define in detail. However, perfect knowledge of the motion of the sensor tip is not necessary to obtain a reasonable measure of χ_T (section 5b). A sampling test conducted to successively reduce the information available from which to compute u indicated that the most important motion sensor is a pressure sensor that resolves the surface wave–induced motion. This, plus a measure of the mean water velocity past the sensor, results in a 27% mean bias in estimates of χ_T.

APPENDIX A

Computation of Flow Speed Past the Sensor

To accurately compute the flow speed past the sensor we must first calculate the velocity of the sensor tip and its orientation at all times, and then properly combine these computations with current measurements. We start with the computation of χpod orientation with respect to the earth using accelerometer, rotation rate, and compass data. Once we know the χpod orientation, we can estimate gravitational components of measured accelerations. In the next step we calculate motion package velocities in BCS by integrating measured accelerations corrected for gravitational signal and then apply
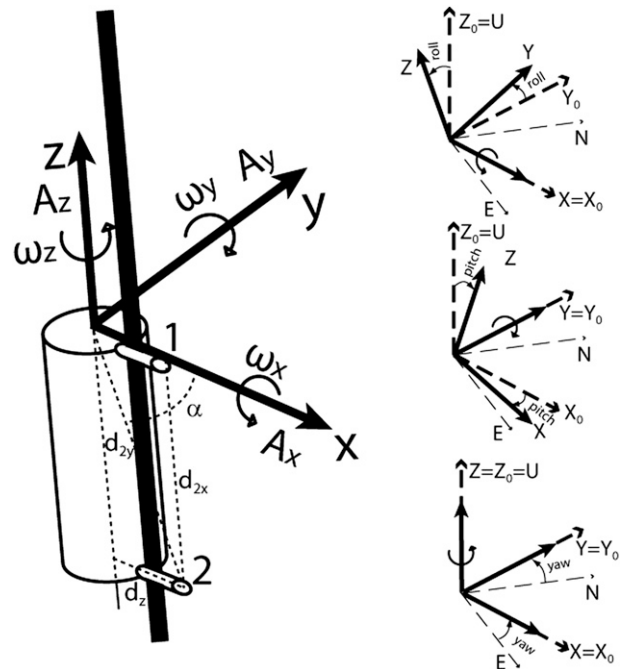

FIG. A1. χpod schematics and axes convention. Accelerations (A_x, A_y, A_z) and angular velocities (ω_x, ω_y, ω_z) refer to BCS. Positive accelerations are in the direction of the corresponding axes and positive rotations are in clockwise direction around the corresponding axes. Here, d_z is distance from axis Z to sensor 1 and 2 (identical), d_{2x} is distance from axis X to sensor 2, and d_{2y} is distance from axis Y to sensor 2; α is the angle between the line running along d_{2y} and the XY plane. The three angles yaw, pitch, and roll give the orientation of the χpod with respect to the earth. Yaw is heading angle, and pitch and roll are defined as χpod's tilts from vertical orientation: pitch is inclination angle (rotation around Y_0), and roll is bank angle (rotation around X_0).

corrections to get sensor tip velocities. Finally, we translate current velocities from the earth's reference frame to BCS and combine them with sensor tip velocities to get flow speed past the sensor. In this demonstration we use a 24-h record.

The χpod's axis convention is shown in Fig. A1. Roll, pitch and yaw angles give the orientation of the χpod with respect to the earth. Yaw is defined as heading angle (in our convention, clockwise rotation around vertical axis from the east), while pitch and roll angles are defined as χpod's tilts from vertical orientation: pitch is inclination angle (clockwise rotation around Y_0 in Fig. A1), and roll is bank angle (clockwise rotation around X_0 in Fig. A1).

a. Calculation of roll, pitch, and yaw

To properly calculate χpod orientation and motion, we need to know the time history of roll, pitch and yaw. The data available from angular rate sensor measurements are angular velocities in BCS. Angles, computed

by integrating these data in time, result in roll, pitch and yaw. Conversion is performed incrementally, which results in rapid error accumulation resulting from noise and drift of the initial signal. If reference positions are well known at intervals that are short compared with error accumulation, then errors are minimized by using Kalman filters (Walchko 2002). While the mooring moves around the same position, there are no well-known reference points of exact χpod locations. Fortunately, in our case pitch and roll angles are small (within a few degrees), and we can assume that rotations measured in BCS are a good proxy for roll, pitch and yaw. That way we have small independent errors at every time step but avoid error accumulation (see Pamadi 2004, p. 332–334).

In practice, we cannot use rotation rate data alone to compute χpod rotations, because rate sensors drift at low frequencies. Because χpod is fixed on a mooring line, low-frequency accelerations represent gravitational accelerations and are attributed to low-frequency instrument tilts. Compass data have minimal low-frequency drift. Thus, χpod rotation angles are computed by combining low-frequency components calculated from accelerometer and compass data with high-frequency components calculated from rate sensor data.

The procedure is as follows. Compass and accelerometer data are twice low passed at 100 s (thereby removing surface wave effects) using a fourth-order Chebychev filter with ripple = 20. Then low-frequency tilts are calculated as

$$\begin{cases} \sin \text{roll}_{\text{lp}} = A_y^{\text{lp}}/g \\ \sin \text{pitch}_{\text{lp}} = -A_x^{\text{lp}}/(g \cos \text{roll}_{\text{lp}}) \end{cases}, \quad \text{(A1)}$$

where A_y^{lp} and A_x^{lp} are low-passed accelerometer signals and roll_{lp} and pitch_{lp} are low-frequency roll and pitch. Low-frequency yaw is low-passed compass data.

Rotation rate sensors not only drift at long time periods, but are noisy at high frequencies. The following sequence of filters is applied to calibrated rate data: data are detrended, high passed at 200 s, detrended, low passed at 1 s, integrated, again high passed at 200 s, and once more detrended. We use a Chebychev fourth-order filter with ripple = 20. High-frequency rotations are then assumed to be a proxy of high-frequency components of roll, pitch, and yaw. Low-frequency and high-frequency rotations are then combined linearly to obtain full χpod rotations.

To perform a robustness check of our rotation calculations, we compared yaw rotations computed from combined rotation rate signal and unfiltered compass
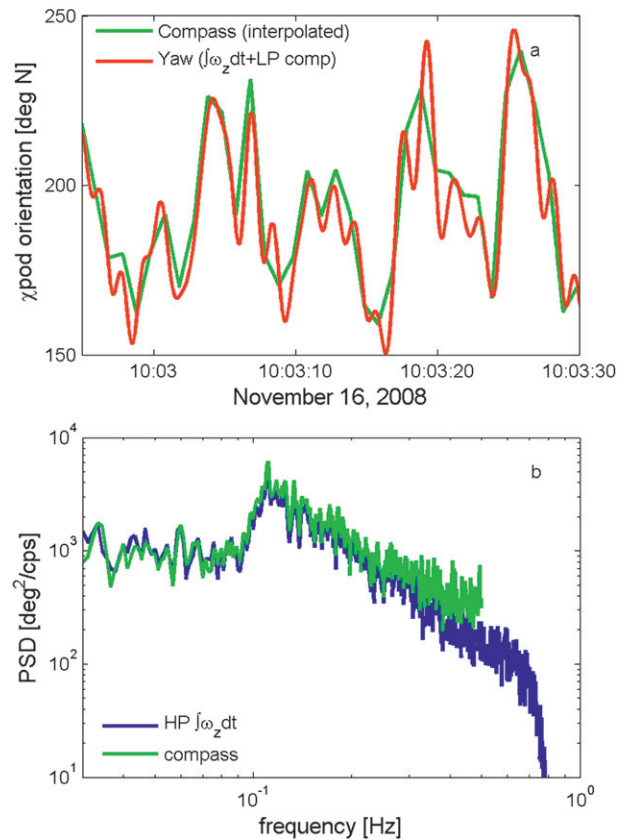

FIG. A2. (a) Instrument orientation measured by compass and computed from rate sensor data (using mean compass offset). (b) Power spectra of integrated high-passed rate data and compass data.

data (Fig. A2). This demonstrates that both signals are very similar, lending some confidence that the procedure works properly also for pitch and roll calculations, for which we cannot perform an independent test.

b. Computation of gravitational components

The gravitational vector in BCS is the vector product of rotational cosine matrix (see appendix B) and gravitational acceleration vector. No gravitational signal is introduced by rotation around the vertical axis (yaw),

$$A_{x,y,z}^g = R_{rpy}(0,0,g) \quad \text{(A2)}$$

or

$$\begin{cases} A_x^g = -g \sin \text{pitch} \cos \text{roll} \\ A_y^g = g \sin \text{roll} \\ A_z^g = g \cos \text{pitch} \cos \text{roll} \end{cases}. \quad \text{(A3)}$$

c. Estimation of χpod velocities

The χpod velocities are calculated in BCS. The coordinate center is located at the motion package, in the upper cap behind sensor 1 (see Fig. A1). The motion package velocity in BCS is the integral of the difference between measured and gravitational accelerations. Because χpod's position is fixed at the mooring line, this constant of integration is zero,

$$
\begin{cases}
u_a = \int (A_x - A_x^g)\,dt \\
v_a = \int (A_y - A_y^g)\,dt\,, \\
w_a = \int (A_z - A_z^g)\,dt
\end{cases}
\tag{A4}
$$

where u_a, v_a, w_a are X, Y, and Z velocity components.

Sensor tips are located away from the coordinate center, so their velocity differs from the velocity of the accelerometer package by χpod's angular velocities. Because the upper sensor lies on axis X, no rotation modifies the u velocity component of the sensor tip as compared to the motion package u velocity; also rotation around X does not modify u and w velocity components. A lower sensor lies in the XZ plane, so rotation around Z does not affect its u velocity component, and rotation around X does not affect its w velocity component,

$$
\begin{cases}
u_{s1} = u_a \\
v_{s1} = v_a + \omega_z d_z, \\
w_{s1} = w_a - \omega_y d_{1y}
\end{cases}
\tag{A5}
$$

$$
\begin{cases}
u_{s2} = u_a - \omega_y d_{2y}\sin\alpha \\
v_{s2} = v_a + \omega_x d_{2x} + \omega_z d_z, \\
w_{s2} = w_a - \omega_y d_{2y}\cos\alpha
\end{cases}
\tag{A6}
$$

where indexes (1, 2) relate to corresponding sensor tip, $d_{x,y,z}$ are the distances between sensor tip and rotation axis, and $\omega_{x,y,z}$ are angular velocities measured at the motion package.[A1]

An evaluation of the uncertainties on χpod velocities related to rotations around X and Y indicates they are much smaller than those related to rotation around Z and do not exceed 3 cm s^{-1} (see Fig. A3). Because these velocity corrections are well within uncertainties in current speed measurements, we neglect them and estimate sensor tip velocity as
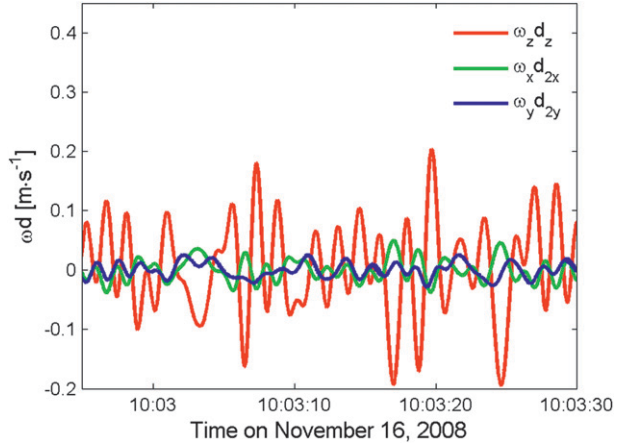

[A1] The subscript s refers to sensor.

FIG. A3. Components of sensor tip velocities related to χpod rotation.

$$
\begin{cases}
u_s = \int (A_x - A_x^g)\,dt \\
v_s = \int (A_y - A_y^g)\,dt + \omega_z d_z. \\
w_s = \int (A_z - A_z^g)\,dt
\end{cases}
\tag{A7}
$$

d. Calculation of flow speed past sensor

Finally, to calculate the speed past the sensor tip, we translate the current velocity vector from the earth's reference frame to BCS using (B5) (from below) and combine it with sensor tip velocity (A7). Then, the flow speed past sensor is given by

$$
u = [(u_s - U^B)^2 + (v_s - V^B)^2 + (w_s - W^B)^2]^{1/2},
\tag{A8}
$$

where U^B, V^B, W^B are components of current speed in BCS.

APPENDIX B

Axes Transformation–Directional Cosine Matrix

Rotation of a given reference frame relative to another reference frame is specified by three Euler angles: yaw, pitch, and roll (Fig. A1). To describe the orientation of BCS with respect to the earth's frame, vector translation for a rotation around one of the axes is done by multiplying the vector by its corresponding directional cosine matrix (DCM; Pamadi 2004).

The yaw cosine matrix is

$$\mathbf{R}_{\text{yaw}} = \begin{bmatrix} \cos\text{ yaw} & \sin\text{ yaw} & 0 \\ -\sin\text{ yaw} & \cos\text{ yaw} & 0 \\ 0 & 0 & 1 \end{bmatrix}, \qquad \text{(B1)}$$

pitch cosine matrix is

$$\mathbf{R}_{\text{pitch}} = \begin{bmatrix} \cos\text{ pitch} & 0 & -\sin\text{ pitch} \\ 0 & 1 & 0 \\ \sin\text{ pitch} & 0 & \cos\text{ pitch} \end{bmatrix}, \qquad \text{(B2)}$$

and roll cosine matrix is

$$\mathbf{R}_{\text{roll}} = \begin{bmatrix} 1 & 0 & 0 \\ 0 & \cos\text{ roll} & \sin\text{ roll} \\ 0 & -\sin\text{ roll} & \cos\text{ roll} \end{bmatrix}. \qquad \text{(B3)}$$

Total body rotation is calculated by multiplying the individual rotations. Note that the order of these rotations is extremely important, because any other order of rotation would normally result in a different orientation. The difference between calculations with different orders of operations is reduced by applying very small rotation increments. We use a yaw → pitch → roll sequence,

$$\mathbf{R}_{\text{rpy}} = \mathbf{R}_{\text{roll}} \times \mathbf{R}_{\text{pitch}} \times \mathbf{R}_{\text{yaw}}. \qquad \text{(B4)}$$

Thus, vector $\mathbf{A}_{\text{ENU}}$ given in the earth coordinate system is translated to BCS as follows:

$$\mathbf{A}_{\text{BCS}} = \mathbf{R}_{\text{rpy}} \times \mathbf{A}_{\text{ENU}}. \qquad \text{(B5)}$$

REFERENCES

Doron, P., L. Bertolucci, J. Katz, and T. R. Osborn, 2001: Turbulence characteristics and dissipation estimates in the coastal ocean bottom boundary layer from PIV data. *J. Phys. Oceanogr.,* **31,** 2108–2134.

Gregg, M. C., H. Peters, J. C. Wesson, N. S. Oakey, and T. J. Shay, 1985: Intensive measurements of turbulence and shear in the Equatorial Undercurrent. *Nature,* **318,** 140–144.

Lien, R., D. R. Caldwell, M. C. Gregg, and J. N. Moum, 1995: Turbulence variability at the equator in the central Pacific at the beginning of the 1991-1993 El Niño. *J. Geophys. Res.,* **100** (C4), 6881–6898.

——, E. D'Asaro, and M. McPhaden, 2002: Internal waves and turbulence in the upper central equatorial Pacific: Lagrangian and Eulerian observations. *J. Phys. Oceanogr.,* **32,** 2619–2639.

Lorke, A., and A. Wuest, 2005: Application of coherent ADCP for turbulence measurements on the bottom boundary layer. *J. Atmos. Oceanic Technol.,* **22,** 1821–1828.

Lueck, R. G., D. Huang, D. Newman, and J. Box, 1997: Turbulence measurement with a moored instrument. *J. Atmos. Oceanic Technol.,* **14,** 143–161.

McPhee, M. G., 1992: Turbulence heat flux in the upper ocean under sea ice. *J. Geophys. Res.,* **97** (C4), 5365–5379.

Moum, J. N., and D. R. Caldwell, 1985: Local influences on shear flow turbulence in the equatorial ocean. *Science,* **230,** 215–315.

——, and J. D. Nash, 2009: Mixing measurements on an equatorial ocean mooring. *J. Atmos. Oceanic Technol.,* **26,** 317–336.

——, M. C. Gregg, R. C. Lien, and M. Carr, 1995: Comparison of turbulence kinetic energy dissipation rate estimates from two ocean microstructure profilers. *J. Atmos. Oceanic Technol.,* **12,** 346–366.

——, J. M. Klymak, J. D. Nash, A. Perlin, and W. D. Smyth, 2007: Energy transport by nonlinear internal waves. *J. Phys. Oceanogr.,* **37,** 1968–1988.

——, R.-C. Lien, A. Perlin, J. D. Nash, M. C. Gregg, and P. J. Wiles, 2009: Sea surface cooling at the equator by subsurface mixing in tropical instability waves. *Nat. Geosci.,* **2,** 761–765, doi:10.1038/NGEO657.

——, J. D. Nash, and W. D. Smyth, 2011: Narrowband high-frequency oscillations at the equator. Part I: Interpretation as shear instabilities. *J. Phys. Oceanogr.,* **41,** 397–411.

Nash, J. D., and J. N. Moum, 1999: Estimating salinity variance dissipation rate from microstructure conductivity measurements. *J. Atmos. Oceanic Technol.,* **16,** 263–274.

Osborn, T. R., 1980: Estimates of the local rate of vertical diffusion from dissipation measurements. *J. Phys. Oceanogr.,* **10,** 83–89.

——, and C. S. Cox, 1972: Oceanic fine structure. *Geophys. Fluid Dyn.,* **3,** 321–345.

Pamadi, B. N., 2004: *Performance, Stability, Dynamics, and Control of Airplanes.* AIAA, 780 pp.

Sun, C., W. D. Smyth, and J. N. Moum, 1998: Dynamic instability of stratified shear flow in the upper equatorial ocean. *J. Geophys. Res.,* **103** (C5), 10 323–10 337.

Walchko, K. J., 2002: Low cost inertial navigation: Learning to integrate noise and find your way. M.S. thesis, Dept. of Electrical and Computer Engineering, University of Florida, 80 pp. [Available online at http://www.mil.ufl.edu/publications/thes_diss/Kevin_Walchko_thesis.pdf.]

Wiles, P. J., T. P. Rippeth, J. H. Simpson, and P. J. Hendricks, 2006: A novel technique for measuring the rate of turbulence dissipation in the marine environment. *Geophys. Res. Let.,* **33,** L21608, doi:10.1029/2006GL027050.

Williams, A. J., J. S. Tochko, R. L. Koehler, T. F. Gross, W. D. Grant, and C. V. R. Dunn, 1987: Measurement of turbulence with an acoustic current meter array in the oceanic bottom boundary layer. *J. Atmos. Oceanic Technol.,* **4,** 312–327.

Zhang, Y., and J. N. Moum, 2010: Inertial-convective subrange estimates of thermal variance dissipation rate from moored temperature measurements. *J. Atmos. Oceanic Technol.,* **27,** 1950–1959.